Dynamic phase imaging and processing of moving biological organisms

Katherine Creath[1,2,3*] and Goldie Goldstein[1,3]
[1]4D Technology Corporation, Tucson AZ 85706,
[2]Optineering, Tucson, AZ USA 85719, and
[3]College of Optical Sciences, The University of Arizona, Tucson, AZ USA 85721

ABSTRACT

This paper describes recent advances in developing a new, novel interference Linnik microscope system and presents images and data of live biological samples. The specially designed optical system enables instantaneous 4-dimensional video measurements of dynamic motions within and among live cells without the need for contrast agents. "Label-free" measurements of biological objects in reflection using harmless light levels are possible without the need for scanning and vibration isolation. This instrument utilizes a pixelated phase mask enabling simultaneous measurement of multiple interference patterns taking advantage of the polarization properties of light enabling phase image movies in real time at video rates to track dynamic motions and volumetric changes. Optical thickness data are derived from phase images after processing to remove the background surface shape to quantify changes in cell position and volume. Data from a number of different pond organisms will be presented, as will measurements of human breast cancer cells with the addition of various agents that break down the cells. These data highlight examples of the image processing involved and the monitoring of different biological processes.

Keywords: phase imaging, interference microscopy, polarization interferometry, cellular imaging, cell dynamics, optical thickness measurement, label-free imaging, 4D microscopy

1. INTRODUCTION

The ability to instantaneously measure live cells, and follow motions and processes over time, provides valuable information to researchers studying cellular dynamics, motility, and cell and tissue morphology. Quantitative phase imaging can measure structures from interference images analogous to those viewed with phase-contrast imaging and differential interference contrast imaging. Phase images can reveal features and quantitative data that are not available through conventional imaging. Phase imaging quantifies optical thickness variations due to small variations in refractive index relating to variations in density of different structures and materials within cells and tissues. Very small refractive index variations can manifest as large variations in optical thickness. Phase image data enable quantitative measurements that aren't possible with standard microscopy techniques. They can be directly combined and correlated with any other type of microscopic imaging such as fluorescence imaging. To obtaining phase image data, harmeless light levels are used, and samples do not need to be stained, labeled or marked. By taking short snapshots in rapid succession, the dimension of time opens up the ability to track motions of cells, see how cells interact with one another, and follow small motions within cells, tissues and structures. This type of imaging enables new types of studies involving cell tracking and process monitoring.

This paper presents an update on current research in developing a novel Linnik interference microscope specially designed for measurement of living and moving biological samples in liquids under coverslips. For the specific work of this project, objects are viewed in reflection; however, the method is easily adaptable to measurement in transmission or for use with immersion. Besides describing the current instrument design, this paper discusses methods of image processing to enable extraction of position and volumetric information and many measurement examples.

* email: kcreath@ieee.org

Three-Dimensional and Multidimensional Microscopy: Image Acquisition and Processing XIX,
edited by Jose-Angel Conchello, Carol J. Cogswell, Tony Wilson, Thomas G. Brown, Proc. of SPIE
Vol. 8227, 82270M · © 2012 SPIE · CCC code: 1605-7422/12/$18 · doi: 10.1117/12.908859

2. BACKGROUND

Techniques developed for full-field phase-imaging interference microscopes have historically relied upon temporal phase-measurement methods, which obtain interferograms sequentially, and therefore require good vibrational damping and static specimens so that high-quality data can be obtained.[1-3] These techniques have been used for biological measurements but have not been utilized as much as they could because most of them are sensitive to motion and vibration. [4-14] Most interferometric microscopes have utilized narrowband illumination with short coherence lengths of tens of microns. The reason for narrowband "low coherence" illumination (short temporal coherence length) is to reduce effects of reflections off of nearby surfaces and to help reduce effects of speckle in the imaging systems. Further improvement in imaging quality can be obtained by incorporating low spatial coherence extended sources. With biological samples, low spatial coherence illumination enables the samples to be isolated in space without getting spurious interference patterns from other surfaces (mainly the coverslip). This section briefly outlines the techniques used in this system. More details can be found in the references. [15-17]

2.1 Dynamic interference microscope system

The interference microscope used for this work is based upon a Linnik configuration.[3] It is comprised of a Köhler-type illumination system utilizing a low coherence extended source,[18] and a simple imaging system as shown in Figure 1. An aperture stop enables controlling the size of the source in the entrance pupil of the microscope objectives, while a field stop enables easier alignment of the system.

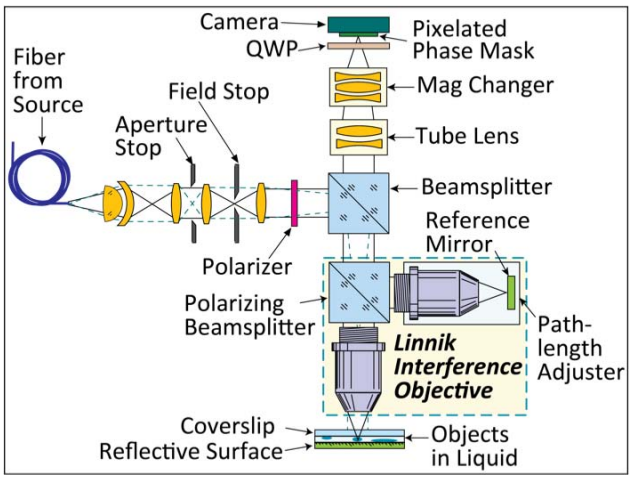

Figure 1. Optical schematic of Linnik interference microscope.

The object and reference beams have orthogonal polarizations with the incoming illumination split into orthogonal polarizations before the microscope objectives using a polarization beamsplitter. The relative irradiances of the test and object beam are balanced for maximum contrast using the polarizer. A quarter-wave plate (QWP) before the camera combines the two polarized beams so that the two beams can interfere at the pixelated phase mask. For the measurements in this paper, samples in water or cell media are viewed in reflection through a cover slip. For the examples presented in this paper, sources with wavelengths of 660 nm and 785 nm were used with 20X NA 0.45, or 10X NA 0.3 (A 50X NA 0.8 is being built). The imaging "tube" lens magnification was either 1X, 1.67X or 2.25X.

Figure 2. Prototype interference microscope.

Figure 2 shows a photograph of the prototype system. The Linnik objective is seen below the microscope (blue and white box) with a 5-axis translation stage below for adjusting position and tip/tilt of the sample. The compact design of this system enables it to be used on a variety of stands so that it can be interfaced with different types of staging and cell handling systems.

2.1.1 Extended low coherence source

Standard practice in interference microscopes would be to use a temporally low coherence source like an LED. However, this reduces the temporal coherence length drastically and would require equal optical paths in both arms of the Linnik so that the temporal coherence function overlaps with the spatial coherence function. [19, 20] Essentially this means that there would also need to be an equivalent amount of glass and liquid in the

reference arm as in the test arm in order to get equal optical path lengths.

To get around this limitation, it has been shown that by tailoring the temporal and spatial coherence, dispersive media can be unmatched in both arms and still have the positive effects of low coherence. [19, 20] This is done by designing the source so that the temporal coherence is long enough to enable path length differences generated by the dispersive media (the cover slip and liquid), while reducing the spatial coherence to localize the interference fringes in space so that spurious reflections and coherent noise are not present.

To reduce the spatial coherence to 25-35 µm, diode laser beams having temporal coherence lengths of 250-300 µm were focused onto a rotating diffuser and then coupled into an NA 0.2 multi-mode optical fiber with a 1000 µm core. The laser has sufficient temporal coherence over path length differences that take into account the cover glass, while the spatial size of the source given by the multi-mode optical fiber will limit the spatial coherence.

2.1.2 Obtaining high quality interference fringes

For a Linnik interference microscope objective, the reference objective and the reference mirror are moved together to match the path lengths in the reference and test arms to maximize fringe contrast. The reference mirror remains in a fixed position relative to the reference objective. When imaging an object, focus is first adjusted on the sample. The entire reference arm (reference microscope objective and reference mirror) is moved to maximize fringe contrast. As long as there is the same coverslip and liquid thickness, the reference pathlength should not need to be readjusted. Further optimization of interference fringe visibility is accomplished by balancing the amount of light in the reference and test beams by rotating the polarizer in the illumination.

Because the objectives used are not designed for coverslips, the coverslip and liquid thickness will generate some spherical aberration in the measurements. However, because it is possible to subtract out small amounts of spherical aberration from measurements, and to also subtract a reference measurement file, there is no noticeable image degredation with magnifications of 50X or lower. With total thicknesses of <0.2 mm, very good fringe contrast is easily obtainable.

2.2 Obtaining phase images and determining optical thickness

For phase imaging applications, pixelated phase mask sensor technology uniquely provides a single frame phase measurement in a compact, robust format that is compatible with conventional microscope imagining systems, and permits the use of a wide variety of wavelengths and source bandwidths without the need for vibration isolation or scanning.[21-23] All necessary information to determine phase is recorded in a single snapshot. It enables the creation of a versatile and compact microscope interferometer for biological applications.

2.2.1 Wire-grid polarizers

The polarization-mask is constructed from an array of micropolarizers that are constructed from wire grid polarizers as shown in Figure 3. Wire-grid polarizers are made of tiny metal wires that are deposited on a transparent substrate (typically aluminum wires on a glass substrate). The linewidth, thickness and period of the wires are approximately 100nm, 120nm and 240nm respectively**.** These sub-wavelength structures have the property of reflecting light polarized parallel to the wires and transmitting light polarized perpendicular to them. They function as efficient polarizers over a wide range of wavelengths and angles.

2.2.2 Phase imaging with a pixelated phase-mask

At the phase mask, the reference and test beams have orthogonal circular polarizations (i.e., right-hand circular and left-hand circular). When combined, the measured irradiance at each pixel of the mask is given by [24]

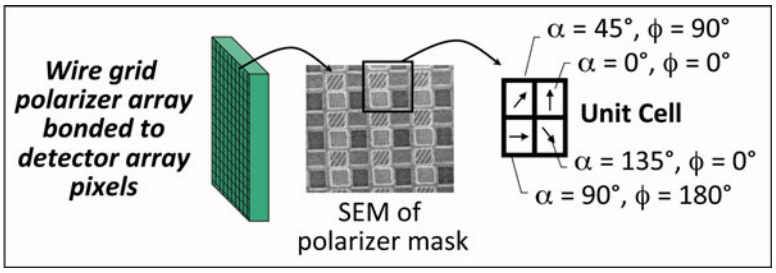

Figure 3. The pixelated phase mask has 4 different polarizations comprising a unit cell of 2x2 different relative phase values.

$$I(x,y) = \frac{1}{2}\left\{ I_r + I_s + 2\sqrt{I_r I_s}\cos\left[\Delta\varphi(x,y) + 2\alpha_p\right]\right\},$$

where α_p is the angle of the polarizer with respect to the *x*, *y* plane, I_r and I_s are the intensity of reference and signal beams respectively, and $\Delta\phi(x,y)$ is the optical path difference between the beams. When this equation is applied to each of the 4 pixels in the unit cell, phase differences of 0°, 90°, 180°, and 270° are encoded into a single image when a single interferogram is recorded. For each of the four pixel types we can write,

$$A(x,y) = \frac{1}{2}\left\{ I_r + I_s + 2\sqrt{I_r I_s}\cos\left[\Delta\varphi(x,y)\right]\right\} \qquad C(x,y) = \frac{1}{2}\left\{ I_r + I_s + 2\sqrt{I_r I_s}\cos\left[\Delta\varphi(x,y) + \pi\right]\right\}$$

$$B(x,y) = \frac{1}{2}\left\{ I_r + I_s + 2\sqrt{I_r I_s}\cos\left[\Delta\varphi(x,y) + \frac{\pi}{2}\right]\right\} \quad D(x,y) = \frac{1}{2}\left\{ I_r + I_s + 2\sqrt{I_r I_s}\cos\left[\Delta\varphi(x,y) + \frac{3\pi}{2}\right]\right\}.$$

Four simultaneous full-field interferograms can then be synthesized by combining pixels of each phase type. These four interferograms can be processed by a variety of algorithms that are well-known for calculating image phase.[25, 26] One well-known phase algorithm is the simple four-frame algorithm,

$$\varphi(x,y) = ATAN\left\{\frac{\left[C(x,y) - A(x,y)\right]}{D(x,y) - B(x,y)}\right\},$$

where ATAN is the arctangent function. This produces a modulo 2π (wrapped) phase map which then needs to be unwrapped using standard techniques.[27, 28] These phase image calculations can be done in real-time.

2.2.3 Determining optical thickness

Each interference fringe in reflection corresponds to one-half wave of optical path difference (OPD – the measured phase difference – or phase – for short). Typically, the raw units of this measure are in terms of wavelengths of the source light (waves). To make these data more useful we convert phase data to optical thickness OT(x,y), given by

$$OT(x,y) = OPD \cdot \frac{\lambda}{2} = \varphi(x,y)\left[\frac{\lambda}{4\pi}\right]$$

Optical thickness (OT) is an integrated measure of the overall optical path through the sample, which is the product of the localized index of refraction n(x,y,z) and the physical thickness t(x,y,z),

$$OT(x,y) = \int_o^T n(x,y,z)\cdot t(x,y,z)dz \cdot$$

For viewing in reflection OT includes a double pass through the coverslip and liquid containing the objects. Denser areas of the object with higher indices of refraction will yield a larger OT as shown in Figure 4. Typically, the index of refraction of the coverslip is ~1.5, the index of water is ~1.33, while cellular media is ~1.37, cytoplasm ~1.39 and cellular organelles like nuclei ~1.41-1.43. Subtle differences as small as the third decimal place in refractive index are detectable by this system.[15-17, 29]

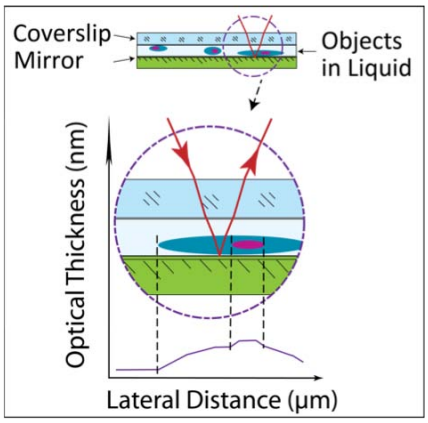

Figure 4. Optical path length through test sample includes the coverslip, liquid and objects. Graph (bottom) shows optical thickness profile for the section within the highlighted area.

2.2.4 Optical performance

This system is designed to have two different fields of view (FOV) using a flip-in FOV lens in the imaging arm. This effectively changes the total system magnification by a factor of 2.25X. With 20X objectives, this yields 20X and 45X. The Illunis XMV-2020 camera in this system has an active area of 9.2 x 8.88 mm yielding a 20X FOV of 460 x 440 µm and 204 x 197 µm at 45X.

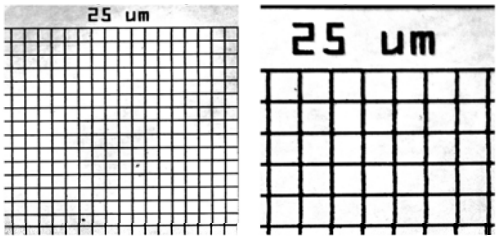

Figure 5. Images of Edmund Optics multi grid standard at 20X and 45X.

Although the FOV lens increases the total system magnification by a factor of 2.25X, the optical resolution remains the same for a given objective. With 20X NA 0.45 objectives, the optical resolution is 0.9 µm (0.61 λ/NA). The sampling at the detector with the 1X tube lens is 0.37 µm and with the 2.25X mag changer, it is 0.16 µm, indicating that with 20X total system magnification the image is sampled close to Nyquist, and with 45X it is slightly oversampled. We are in the process of building a 50X NA 0.8 Linnik that will enable optical resolution of 0.5 µm with FOV's of 230 x 170 µm at 50X and 100 x 75 µm and samplings of 0.15 and 0.066 µm. This will significantly improve our measurement resolution and the range of objects that we can measure.

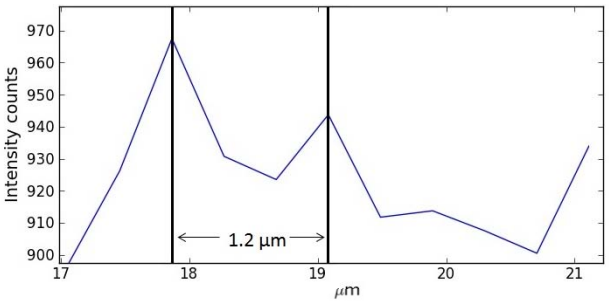

Figure 6. Cross-section profile of ferritin molecules having a separation of 1.25 μm at 20X.

To illustrate the relative fields of view, Figure 5 shows images of an Edmund Optics multigrid standard. The area has been cropped to provide a square FOV. Figure 6 shows a cross section of an image taken of a Ferritin Resolution Standard (Ted Pella, Cat. #608) having ferritin molecules with separations of 1.25 µm. Given the sampling of the image at 20X, there are basically 4 pixels between ferritin molecules. The vertical lines indicate two adjacent ferritin molecules having a separation of ~1.2 µm. These molecules are clearly resolvable at 20X.

2.2.5 Effects of coherent and incoherent imaging

Earlier in this paper we discussed the importance of tailoring the spatial and temporal coherence. Figure 7 illustrates the effect of using a rotating diffuser to improve illumination. Speckle from a 300 µm coherence length diode laser source can be seen in the left images. This coherence length ensures we are not seeing interference from nearby surfaces, but there is still obviously coherence noise present. The right images show improvement by introducing a rotating diffuser. The diffuser fills the entire NA 0.2 and therefore more modes of the multi-mode fiber.

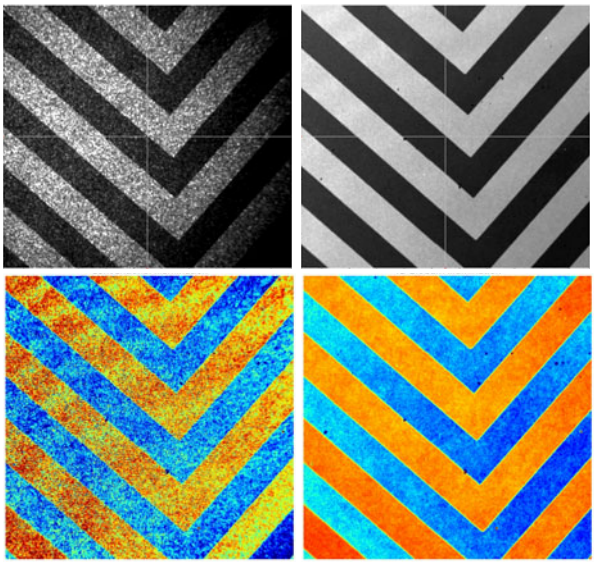

Figure 7. Irradiance (top) and phase (bottom) images of VLSI step height standard taken with (left) diode laser source, and (right) with addition of rotating diffuser.

The illumination falls off in the upper left image because the illumination system is designed assuming a NA 0.2 input that is not completely filled without using the diffuser. When the diffuser is rotated at a high speed, speckle will be averaged out to eliminate the coherent noise and generate a uniform extended source. This type of imaging is typically used in commercial interferometers for optical testing such as Fizeau and Twyman-Green interferometers, but has rarely been used in interference microscopes. This is because interference microscopes typically use temporally less coherence sources than those required to deal with biological object dispersion. Holographic microscopes use more coherent illumination in order obtain sufficent fringe contrast. Clearly, the approach used in this project improves image quality and provides a spatially incoherent image. The improvement

is even more noticeable in phase measurements. Figure 8 shows a single cross section profile through the phase measurements shown in the bottom of Figure 7. The noise in the phase is significantly reduced with the rotating diffuser.

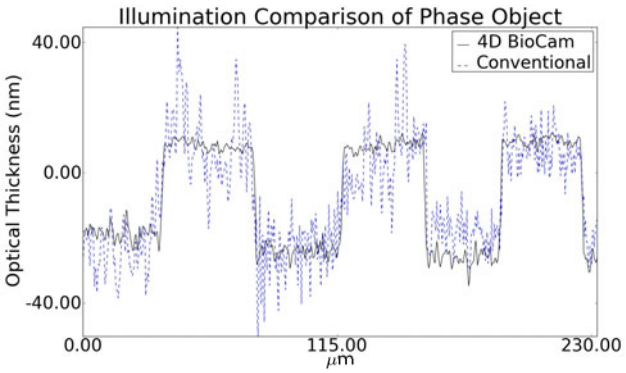

Figure 8. Solid black line shows a cross section through a phase measurement using the rotating diffuser, whereas the dotted blue line is a measurement using a diode laser source without the diffuser.

3. SAMPLE MEASUREMENTS

3.1 Bright Field, interference and phase images

The pixelated phase mask sensor enables three different types of images to be obtained simultaneously as illustrated in images of a rotifer in Figure 9. When the values of all 4 types of pixels are averaged a bright field image is obtained (top left). When values from one type of pixel are displayed, an interferogram or phase-contrast image is obtained (top right). Combining all 4 pixels using the above equations produces a phase image or optical thickness map. Contour and 3D representations of the calculated phase are shown in the bottom images. These were taken at 10X with a 785 nm source. The optical thickness of this sample is about 1200 nm maximum (red) to minimum (blue)(peak-to-valley or P-V). Note that the internal organs are readily visible.

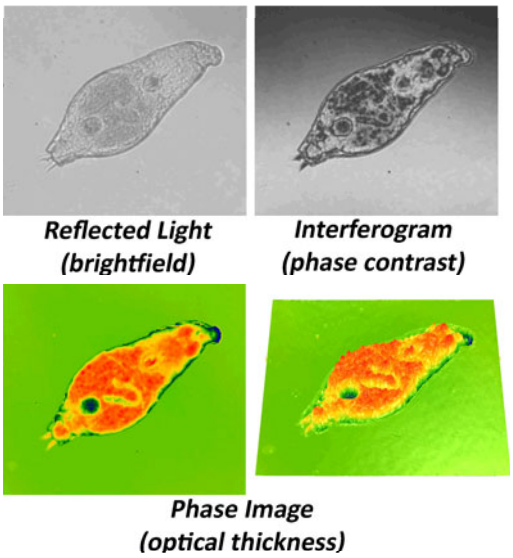

Figure 9. Images of a rotifer. (top left) Brightfield. (top right) Interferogram. (bottom left) Phase image showing optical thickness. (bottom right) 3D view of phase.

3.2 Background removal

In order to obtain quantitative optical thickness data for the extraction of positional motion and/or volumetric changes, the objects of interest must be isolated from the background. Background removal is particularly difficult when there are a few large or numerous smaller objects that are changing within the field of view. One method that can be used for background suppression is to fit low-order Zernike polynomials [26, 30] to the phase data across the entire array, generate a synthetic surface from the Zernike fit and subtract it from the original data. The difference between the data and the Zernike surface effectively isolates the objects and subtracts the low spatial frequency shape of the background surface.

This process serves two functions. Besides removing the background shape so that objects can be quantified relative to a flat surface, the mean value can be kept constant from frame to frame to aid in tracking quantitative changes with time. Figure 10 (Video 1) illustrates this process on 3 frames of a sequence of images from a phase movie taken at 45X of a moving paramecium. Tilt and subtle shape are noticeable in the top images where the left side of the images is higher than the right side. This is removed in the bottom set of images enabling the isolation of the paramecium by itself. Another byproduct of this procedure is

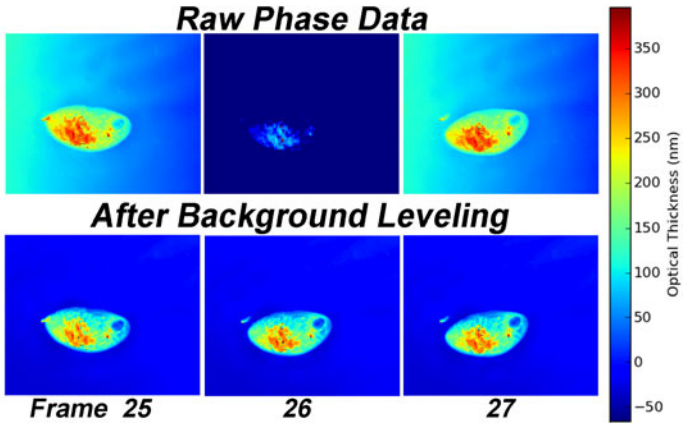

Figure 10. (top) Raw phase data. (bottom) After background subtraction. Video 1. http://dx.doi.org/12908859.1

removal of the mean value from frame to frame. This effectively eliminates jumps between frames caused by noisy pixels, small pieces of debris in the cell solution or scratches on the mirror. Video 1 (Figure 10) illustrates the processing of dynamic data presenting the brightfield data, the interference data, the unprocessed raw phase and then the processing optical thickness data.

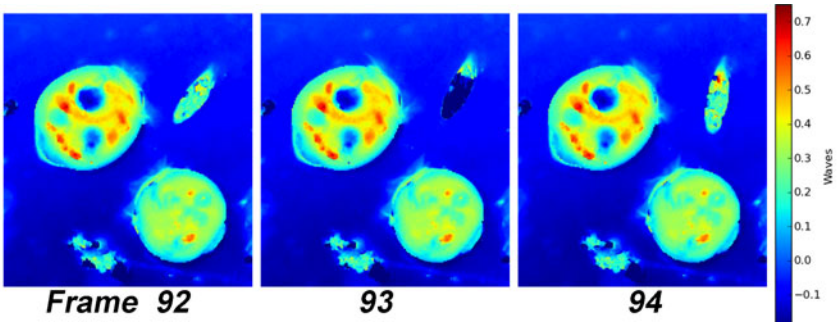

Figure 11. Coleps and paramecium images taken at 20X with 660 nm source. Frames are 0.1 seconds apart in time. The larger coleps is ~60 μm long. The optical thickness scale goes from 460 to -70 nm.

3.3 Phase unwrapping

Another aspect of processing phase data is that since the arctangent function is modulo 2π, the phase values need to be unwrapped. [26, 30] Unwrapping is accomplished by comparing adjacent pixels in the image and adding or subtracting integer multiples of 2π until the phase difference between adjacent pixels is less than π. This constraint limits the slopes that are measureable between adjacent pixels. It also means that noisy data points with low fringe modulation can cause errors in the phase unwrapping. An example of steep slopes affecting unwrapping can be seen in Figure 9. The edges of the rotifer body appear to go below the mean value because of phase unwrapping errors in the pixels around the edge of the rotifer body. There are ways in which unwrapping algorithms can be made more robust, [28, 31] and we will be exploring these as part of our future research.

Phase unwrapping can also affect the relative phase of isolated objects as seen in Figure 11. In this image sequence, the paramecium fails to unwrap consistently in the center frame due to a noisy pixel.

3.4 Breast cancer cell culture example

To show images of in vitro cell cultures the MCF715 human breast cancer line was grown in cell media on coverslips at the University of Arizona Cancer Center. For these images, the coverslips were placed upsidedown on a highly reflective mirror with cell media filling in between the mirror and coverslip. These images were taken at 20X with a 1.67X tube lens, a 660 nm source and 2 ms exposures. Figure 12 shows an image of some of these cells. Note that the intercellular matrix and newly forming cells around the edges of the matrix are clearly visible and easily resolved as are organelles and nuclei within the cells. The lateral sampling in the image for this exposure is 0.53 µm for each 4-pixel 2x2 cell in the pixelated phase mask. The optical resolution at NA=0.45 is 0.9 µm (0.61 λ/NA) yielding a slightly oversampled image. To process this image so that different optical thickness layers have different colors, the background shape due to the mirror and coverslip has been subtracted out by fitting piston, tilt, curvature and cylinder (basically removing a best fit 2nd-order polynomial surface) from the areas where there are not cells present.[26]

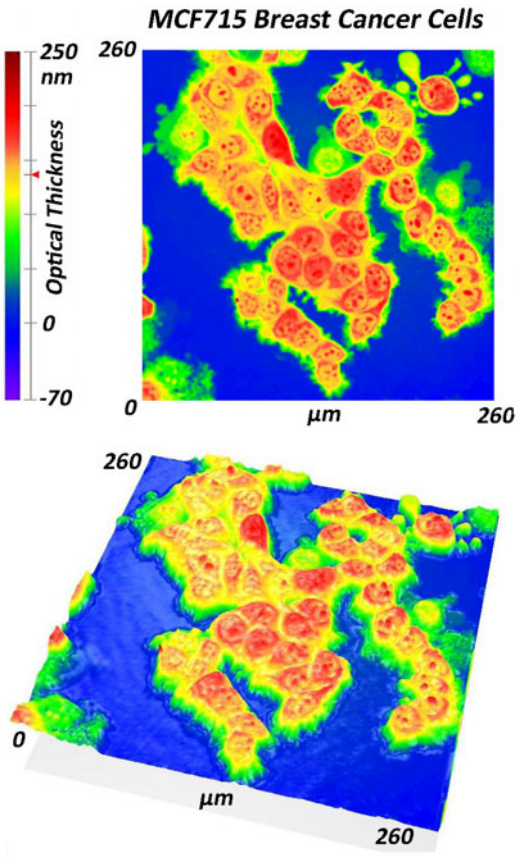

Figure 12. Phase images showing contour and 3D view of human breast cancer cells. Notice cells and matrix forming that look fuzzy without organelles.

3.5 Examples of dynamic motion of ciliates

Many simple organisms were cultured from mud puddles and imaged with this system. Figure 14 shows a series of images from a 40-frame movie taken at 15 Hz. These images have a magnification of 45X with a 660 nm source. Note that the cilia are visible. The paramecium is 10 µm wide and 25 µm long. Another example with a coleps is shown in Figure 13. This protozoa is physically restricted in the liquid layer between the reflective mirror and the cover glass, and unable to swim. Cilia are also clear in this movie, but they are moving fast enough to blur a little with a 1 ms exposure.

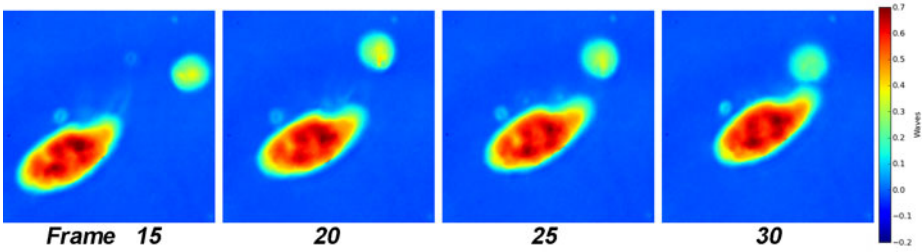

Figure 14. Paramecium interacting with particle at 46X with 660 nm source. Note cilia. The optical thickness scale goes from 460 to -130 nm.

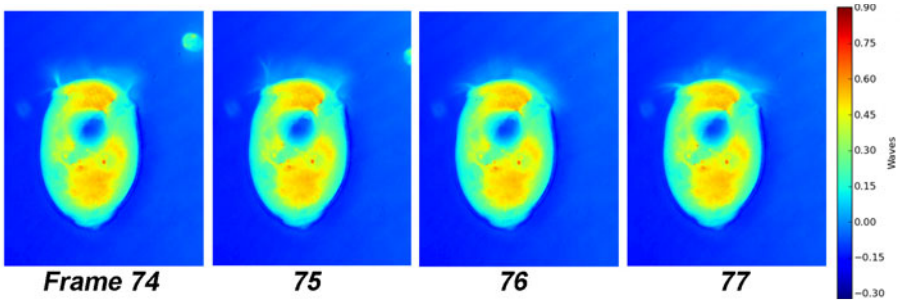

Figure 13. Frames from movie of coleps taken at 46X with a 660 nm source. FOV is 84 x 104 μm. The optical thickness scale goes from 600 to -200 nm.

3.6 Dynamic studies of in vitro cell cultures

Figure 15 shows some images of another cell culture of human breast cancer cells after contact with various media. All of these images are scaled in optical thickness to the same limits of -100 to 450 nm so that changes are more obvious. In Figure 15(A) the cells are in their growth media. In Figure 15(B) the cells have been exposed to purified water causing them to osmotically swell. Figure 15(C) shows how they further swell and flatten after further exposure to purified water while Figure 15(D) shows the cells after then being exposed to NaOH. For each of these cases, 4D phase movies were recorded showing changes every few seconds. Changes are obvious as seen in these few images.

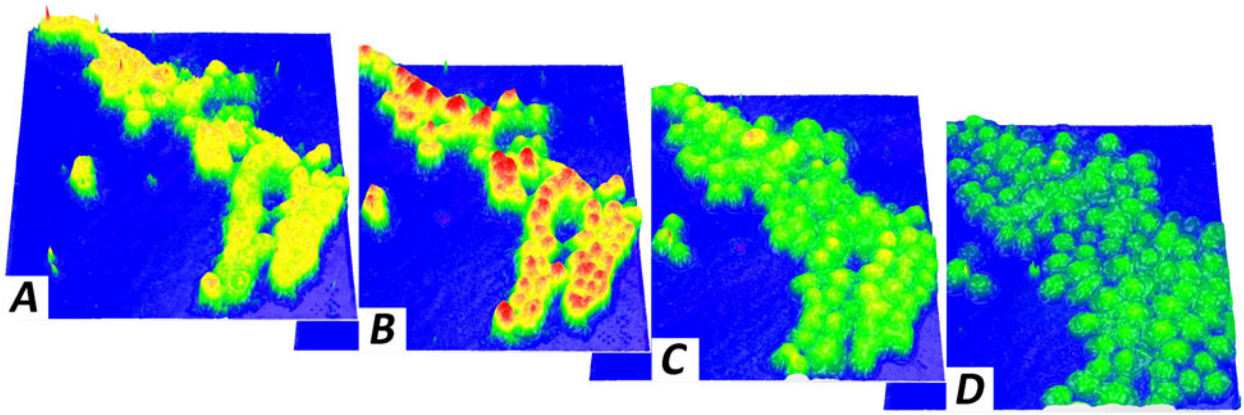

Figure 15. 4D time series of 3D phase images of another breast cancer cell culture. All images have the same optical thickness pseudocolor scale from -100 to 450 nm. (A) Cells in original media. (B) After contact with purified water the cells osmotically swell. (C) After more purified water the cells continue to swell and flatten. (D) After contact with NaOH the cells are beginning to break down. Processes can be monitored with specified time delays as short as 30 frames per second. These are a sampling of movies taken with sampling times of a few seconds over several minutes.

4. DISCUSSION AND CONCLUSIONS

This paper has described recent research into development of a dynamic phase imaging microscope and shown a number of examples of 4D phase measurements of living biological organisms. Short exposure times freeze motion instantaneously. All the data to determine phase and optical thickness can be gathered in a single snapshot, so no scanning is necessary. Data from brightfield imaging and phase contrast (interference image) are also obtained simultaneously along with phase and optical thickness. This model can also be extended to higher magnifications, immersion objectives, higher numerical apertures, a large range of wavelengths, and viewing cells in transmission as well as reflection. Harmless light levels offer a non-destructive means of observing and quantifying biological behavior and dynamic variations over time. The ability to dynamically measure biological organisms in real time opens up many different types of applications ranging from flow cytometry to tissue dynamics, morphological and volumetric studies along with mechanistic studies, process monitoring, quantification of cellular motion, monitoring and tracking cellular damage under known perturbations, tracking cell migration, nerve and muscle transmission, histology and photodynamic therapy. Conceptually, this model could be further modified to include simultaneous fluorescence measurements to more specifically track particular mechanisms.

5. ACKNOWLEDGEMENTS

The authors wish to acknowledge our 4D Technology colleagues Tim Horner and Mark McKune for design of the Linnik and prototype interferometer, Richard Robinson for electrical design, Neal Brock for new technology development, and James Millerd as co-PI on this project. We also wish to thank our University of Arizona collaborator Dr. Andrew Rouse of the Department of Radiology for cell samples. This work has been partially supported by NIH/NCRR 1R43RR028170-01, 2R44RR028170-02, and NIH/NIGMS 8 R44 GM103406-03.

6. REFERENCES

[1] Sommargren, G. E., "Optical Heterodyne Profilometry," Applied Optics **20**, 610-618 (1981).

[2] Wyant, J. C., Koliopoulos, C. L., Bhushan, B., and George, O. E., "An optical profilometer for surface characterization of magnetic media," ASLE Trans. **27**, 101-113 (1984).

[3] Schmit, J., Creath, K., and Wyant, J. C., "Ch. 15. Surface Profilers, Multiple Wavelength, and White Light Interferometry," in [*Optical shop testing; 3rd Edition*], Malacara, D., ed., Wiley-Interscience, Hoboken, N.J., 667-755, (2007).

[4] Dunn, G. A., and Zicha, D., "Phase-Shifting Interference Microscopy Applied to the Analysis of Cell Behaviour," Symposia of the Society for Experimental Biology **47**, 91-106 (1993).

[5] Zicha, D., and Dunn, G. A., "AN IMAGE-PROCESSING SYSTEM FOR CELL BEHAVIOR STUDIES IN SUBCONFLUENT CULTURES," Journal of Microscopy-Oxford **179**, 11-21 (1995).

[6] Eppich, B., Beuthan, J., Dressler, C., and Muller, G., "Optical phase measurements on biological cells," Laser Physics **10**(2), 467-477 (2000).

[7] Tychinsky, V. P., Kretushev, A. V., Klemyashov, I. V., Vyshenskaya, T. V., Filippova, N. A., Raikhlin, N. T., and Shtil, A. A., "Quantitative real-time analysis of nucleolar stress by coherent phase microscopy," Journal of Biomedical Optics **13**(6), 064032 (2008).

[8] Yang, C., Wax, A., Hahn, M. S., Badizadegan, K., Dasari, R. R., and Feld, M. S., "Phase-referenced interferometer with subwavelength and subhertz sensitivity applied to the study of cell membrane dynamics," Optics Letters **26**(16), 1271-1273 (2001).

[9] Popescu, G., "Quantitative Phase Imaging of Nanoscale Cell Structure and Dynamics," in [*Methods in Nano Cell Biology, Volume 90*], Jena, B. P., ed., Elsevier, San Diego, 87-115, (2008).

[10] Hogenboom, D. O., DiMarzio, C. A., Gaudette, T. J., Devaney, A. J., and Lindberg, S. C., "Three-dimensional images generated by quadrature interferometry," Optics Letters **23**(10), 783-785 (1998).

[11] Rockward, W. S., Thomas, A. L., Zhao, B., and DiMarzio, C. A., "Quantitative phase measurements using optical quadrature microscopy," Applied Optics **47**(10), 1684-1696 (2008).

[12] Reed, J., Frank, M., Troke, J. J., Schmit, J., Han, S., Teitell, M. A., and Gimzewski, J. K., "High throughput cell nanomechanics with mechanical imaging interferometry," Nanotechnology **19**(23), (2008).

[13] Ross, G. J., Bigelow, A. W., Randers-Pehrson, G., Peng, C. C., and Brenner, D. J., "Phase-based cell imaging techniques for microbeam irradiations," Nuclear Instruments & Methods in Physics Research Sec B **241**(1-4), 387-391 (2005).

[14] Yu, L. F., Mohanty, S., Liu, G. J., Genc, S., Chen, Z. P., and Berns, M. W., "Quantitative phase evaluation of dynamic changes on cell membrane during laser microsurgery," Journal of Biomedical Optics **13**(5), (2008).

[15] Creath, K., "Dynamic quantitative phase images of pond life, insect wings, and in vitro cell cultures," in [*The Nature of Light: Light in Nature III, SPIE Proc. 7782*], Creath, K., and Shaw, J., eds., SPIE, Bellingham, WA, 77820B, (2010).

[16] Creath, K., "Dynamic phase imaging utilizing a 4-dimensional microscope system," Proc. SPIE **7904**, 79040O (2011).

[17] Creath, K., "Dynamic Phase Imaging for in Vitro Process Monitoring and Cell Tracking," Proceedings of the 33rd Annual International Conference of the IEEE EMBS, Boston, Ma, August 29-September 3, 2011 **33**, 5977-5980 (2011).

[18] Born, M., and Wolf, E., [*Principles of Optics*], Pergamon Press, Oxford, (1975).

[19] Abdulhalim, I., "Competence between spatial and temporal coherence in full field optical coherence tomography and intererence microscopy," J Opt A: Pure Appl. Opt. **8**, 952-958 (2006).

[20] Ryabukho, V., and Lyakin, D., "Longitudinal pure spatial coherence of a light field with wide frequency and angular spectra," Optics Letters **30**(3), 224-226 (2005).

[21] Brock, N. J., Millerd, J. E., Wyant, J. C., and Hayes, J. B., "Pixelated phase-mask interferometer ", USPTO, ed., 4D Technology Corporation, United States, (2007).

[22] Kimbrough, B. T., "Pixelated mask spatial carrier phase shifting interferometry algorithms and associated errors," Applied Optics **45**(19), 4554-4562 (2006).

[23] Novak, M., Millerd, J., Brock, N., North-Morris, M., Hayes, J., and Wyant, J., "Analysis of a micropolarizer array-based simultaneous phase-shifting interferometer," Applied Optics **44**(32), 6861-6868 (2005).

[24] Kothiyal, M. P., and Delisle, C., "Shearing interferomter for phase-shifiting interferometry with polarization phase-shifter," Applied Optics **24**(24), 4439-4442 (1985).

[25] Creath, K., "Phase-measurement interferometry techniques," in [*Progress in Optics*], Wolf, E., ed., Elsevier Science Publishers, Amsterdam, 349-393, (1988).

[26] Malacara, D., ServÌn, M., and Malacara, Z., [*Interferogram analysis for optical testing*], Taylor & Francis, Boca Raton, FL, (2005).

[27] Robinson, D. W., "Phase unwrapping methods," in [*Interferogram Analysis*], Robinson, D. W., and Reid, G. T., eds., IOP Publishing, Bristol, 194-229, (1993).

[28] Ghiglia, D. C., and Pritt, M. D., [*Two-Dimensional Phase Unwrapping: Theory, Algorithms and Software*], Wiley-Interscience, New York, (1998).

[29] Creath, K., and Schwartz, G. E., "Dynamic visible interferometric measurement of thermal fields around living biological objects," in [*Interferometry XII: Techniques and Analysis, Proc SPIE*], Creath, K., and Schmit, J., eds., SPIE, Bellingham, WA, 24-31, (2004).

[30] Malacara, D., [*Optical shop testing*], Wiley-Interscience, Hoboken, N.J. :, (2007).

[31] Ettl, P., and Creath, K., "Comparison of phase-unwrapping algorithms by using gradient of first failure," Applied Optics **35**(25), 5108-5114 (1996).